Supplementary Material

Mechanically-Tunable Quantum Interference in Ferrocene-based Single-Molecule Junctions

María Camarasa-Gómez,[1] Daniel Hernangómez-Pérez,[1,2] Michael S. Inkpen,[3] Giacomo Lovat,[3] E-Dean Fung,[3] Xavier Roy,[4] Latha Venkataraman,[3,4] and Ferdinand Evers[1]

[1]*Institute of Theoretical Physics, University of Regensburg, 93040 Regensburg, Germany*

[2]*Department of Materials and Interfaces, Weizmann Institute of Science, Rehovot 761001, Israel*

[3]*Department of Applied Physics and Applied Mathematics, Columbia University, New York, New York 10027, United States*

[4]*Department of Chemistry, Columbia University, New York, New York 10027, United States*

Email: inkpen@usc.edu; lv2117@columbia.edu; ferdinand.evers@ur.de;

CONTENTS

Synthetic details 2

Measurement Details 4

Ab-Initio calculations details 4

Additional data 6

Orbital symmetry analysis 10

NMR spectra 12

References 14

SYNTHETIC DETAILS

All reactions were conducted in oven-dried glassware under a nitrogen or argon atmosphere, though no special precautions were taken to exclude air or moisture during workup and purification. The preparation of 1, 3-bis(tri[n-butyl]stannyl)ferrocene followed literature methods.[1] Stannylated precursors were purified using alumina, Brockmann grade II. Stille[2, 3] and Negishi[4, 5] conditions were based on previous reports. Zinc chloride and cesium fluoride were dried immediately prior to use by heating under vacuum at 140°C overnight[5] or at 100°C for 2.5 h[6], respectively. Anhydrous and deoxygenated THF was prepared by elution through a dual-column solvent system (MBraun SPS). All other materials were commercially available and used as received. Reported methods are unoptimized, with some yields also impacted by closely eluting impurities (particularly in the isolation of **1,3-Fe**) that reduced the efficiency of purification attempts using column chromatography.

^{1}H and ^{13}C{^{1}H} NMR spectra were recorded on a Bruker Avance III 400, 400SL (400 MHz), or 500 (500 MHz) spectrometer and referenced to the residual solvent peaks of CD_2Cl_2 at δ 5.32 (^{1}H) and 53.84 (^{13}C{^{1}H}) ppm. Mass spectrometry analyses were conducted by Brandon Fowler of the Mass Spectrometry Facility, Chemistry Department, Columbia University, New York using a Waters XEVO G2-XS QToF mass spectrometer.

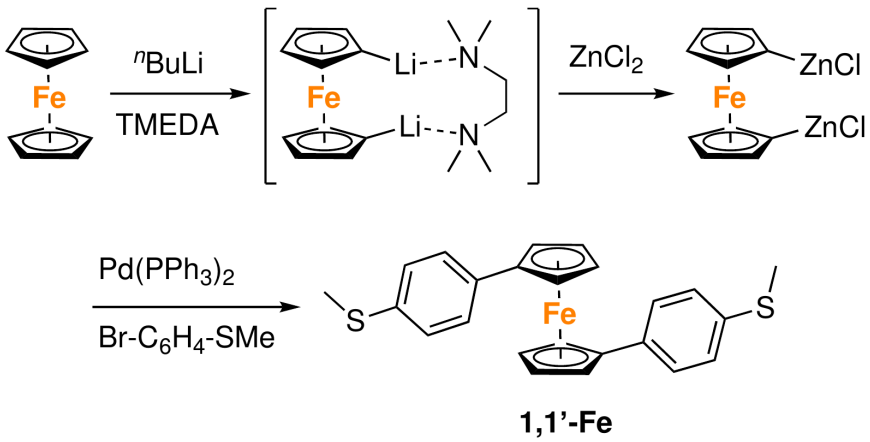

1,1'-Fe

Scheme 1. Synthetic route to **1,1'-Fe** (TMEDA = N,N,N,N'-tetramethylethanediamine).

Synthesis of 1,1'-Fe:

TMEDA (1.66 mL, 11.1 mmol) and 2.5 M n-BuLi in hexanes (4.76 mL, 11.9 mmol) were added to a stirred suspension of ferrocene (1.006 g, 5.407 mmol) in n-pentane (20 mL) held

at 0°C (ice bath). After stirring overnight to room temperature, the majority of solvent was removed by cannula filtration and the orange slurry dissolved in THF (16 mL) at 0°C. A freshly prepared solution of ∼ 0.97 M ZnCl in THF (11.4 mL, ∼ 11.1 mmol) was added, and the mixture was stirred at room temperature for 2.5 h. $Pd(PPh_3)_4$ (0.756 g, 0.654 mmol) and 4-bromothioanisole (2.419 g, 11.91 mmol) were added against nitrogen and the reaction was stirred at 60°C for 18 h. After cooling to room temperature, solvent was removed in vacuo. The crude product was pre-absorbed on SiO_2 and purified by column chromatography, eluting with CH_2Cl_2-hexanes (0 : 100 → 30 : 70 v/v). **1,1'-Fe** was isolated as an orange solid from fractions of the second major orange band (0.961 g, 41%).

^{1}H NMR (400 MHz, CD_2Cl_2): δ (ppm) 2.49 (s, 6H, -SCH_3), 4.21 (pseudo-t, 4H, J = 1.87 Hz, Cp-H), 4.46 (pseudo-t, 4H, J = 1.87 Hz, Cp-H), 7.05 (m, 4H, Ar-H), 7.18 (m, 4H, Ar-H). ^{13}C{^{1}H} NMR (101 MHz, CD_2Cl_2): δ (ppm) 16.19 (2C, -SCH$_3$), 67.91 (4C, Cp C-H), 70.74 (4C, Cp C-H), 86.15 (2C, Cp C-Ar), 126.66 (4C, Ar C-H), 126.94 (4C, Ar C-H), 135.19 (2C, Ar C-R), 136.02 (2C, Ar C-R). HRMS (ASAP+): m/z 431.0590 ([M+H]$^+$ calc. for $C_{24}H_{23}FeS_2$: 431.0591).

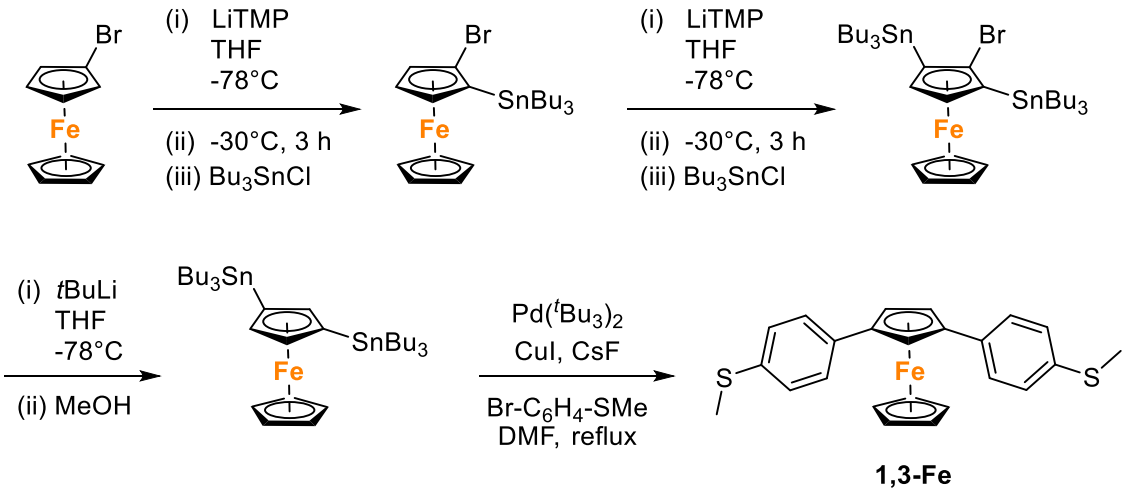

Scheme 2. Synthetic route to **1,3-Fe**.

Synthesis of 1,3-Fe:

1,3-Bis(tri[n-butyl]stannyl)ferrocene (0.361 g, 0.472 mmol), 4-bromothioanisole (0.229 g, 1.13 mmol), CuI (0.009 g, 0.05 mmol), $Pd(t\text{-}Bu_3)_2$ (0.012 g, 0.023 mmol) and DMF (3 mL) were added against nitrogen to dry CsF (∼ 0.184 g, ∼ 1.21 mmol), and stirred at 100°C for 22 h. The cooled mixture was extracted into CH_2Cl_2 and H_2O, whereby the organic layer was filtered through Celite. After solvent removal the crude solid material was pre-

absorbed on SiO_2 and purified by column chromatography, eluting with CH_2Cl_2-hexanes ($0:100 \rightarrow 20:80$ v/v). **1,3-Fe** was isolated as an orange solid from selected fractions of the third orange band (0.006 g, 3%).

^{1}H NMR (400 MHz, CD_2Cl_2): δ (ppm) 2.50 (s, 6H, -SCH_3), 3.90 (s, 5H, Cp-H), 4.79 (d, 2H, J = 1.47 Hz, Cp-H), 5.12 (t, 1H, J = 1.47 Hz, Cp-H), 7.22 (m, 4H, Ar-H), 7.48 (m, 4H, Ar-H). ^{13}C{^{1}H} NMR (101 MHz, CD_2Cl_2): δ (ppm) 16.13 (2C, -SCH$_3$), 64.91 (1C, Cp C-H), 67.46 (2C, Cp C-H), 71.57 (5C, Cp C-H), 86.17 (2C, Cp C-Ar), 126.83 (4C, Ar C-H), 127.04 (4C, Ar C-H), 136.24 (2C, Ar C-R), 136.33 (2C, Ar C-R). HRMS (ASAP+): m/z 431.0587 ([M+H]$^+$ calc. for $C_{24}H_{23}FeS_2$: 431.0591)

MEASUREMENT DETAILS

We measured the conductance of single-molecule junctions formed with two gold electrodes using a custom-built modified Scanning Tunneling Microscope (STM).[7] We used 0.25 mm diameter cut gold wire (99.95%, Alfa Aesar) as the STM tip and 100 nm gold-coated (99.999%, Alfa Aesar) steel pucks as substrates. A commercially available single-axis piezoelectric positioner (Nano-P15, Mad City Labs) was used to achieve sub-angstrom level control of the tip-substrate distance. The STM was controlled using a custom written program in IgorPro (Wavemetrics, Inc.) and operated in ambient conditions at room temperature. The gold substrates were cleaned using a UV/ozone cleaning lamp for 20 minutes prior to use. For each measurement, 1000 traces were first collected prior to adding molecular solutions to check the cleanliness of the gold surface. Solutions of the target molecules at $0.1-1$ mM concentration in tetradecane (Alfa Aesar, 99% purity) or 1,2,4-trichlorobenzene (SigmaAldrich or Alfa Aesar, 99% purity) were added to the substrate for STM break-junction measurements. After the formation of each Au-Au junction with a conductance greater than 5 G_0, the piezoelectric positioner moved the substrate at a speed of 20 nm/s to break the junction. The current and voltage across the junction were acquired at 40 kHz.

AB-INITIO CALCULATIONS DETAILS

Ab-initio calculations were carried out using the closed-shell Kohn-Sham formulation of density functional theory implemented in the FHI-aims code[8]. A non-empirical general-

ized gradient-corrected approximation (PBE) for the exchange-correlation functional[9] was considered. Scalar relativistic corrections to the kinetic energy were incorporated in our first-principles calculations at the atomic zeroth-order regular approximation (ZORA) level[10]. The Kohn-Sham states were represented in an optimized all-electron numeric atom-centered basis set ('tight' computational settings, roughly equivalent to "double zeta + polarization" quality for the molecular atoms and "double zeta quality for the gold atoms which belong to the electrodes). The ground state was obtained using standard convergence criteria in the self-consistent field cycle for the difference in the particle density (10^{-5} electrons/Å^3), total energy (10^{-6} eV), sum of Kohn-Sham eigenvalues (10^{-4} eV) and forces (10^{-4} eV/Å).

The geometries of the molecular junctions were obtained using a well-established two-step process. In the first step, the positions of the molecular atoms and the tip of the electrodes were optimized using the trust-radius enhanced version of the Broyden-Fletcher-Shanno-Goldfarb algorithm[8]. The pyramidal gold clusters used for this geometry optimization contain up to 11 gold atoms per pyramid. Based on test optimizations, we also constrain the S-Me dihedral angle so that the methyl group lies in the same plane as the functionalized phenyl rings. In the second step, the resulting molecular and tip geometries were fixed and additional layers of gold atoms added to the external planes of the previously optimized electrode tips to ensure screening of the excess charge (and therefore, correct level alignment) in the subsequent quantum transport calculations. All the molecular and junction geometries studied in this work were considered to be structurally relaxed when no force component per atom exceeded the threshold value of 10^{-2} eV/Å.

The energy-dependent electronic transmissions were calculated in the regime of linear response using the non-equilibrium Green's function formalism as implemented in the transport package AITRANSS[11, 12]. Each junction electrode was modeled by a pyramidal cluster of 55 atoms with closest interatomic distance of 2.88 Å. The latter cluster was cut along the (111) direction. The self-energy of the reservoirs was parametrized by an energy-independent (Markovian) spatially local function, $\Sigma(\mathbf{r}, \mathbf{r}') = i\eta(\mathbf{r})\delta(\mathbf{r} - \mathbf{r}')$ with non-zero values only in the subspace associated to the outermost layers of the finite cluster. The local absorption rate, $\eta(\mathbf{r})$, was adjusted to guarantee that the electronic transmission remained invariant under smooth moderate changes in $\eta(\mathbf{r})$.

ADDITIONAL DATA

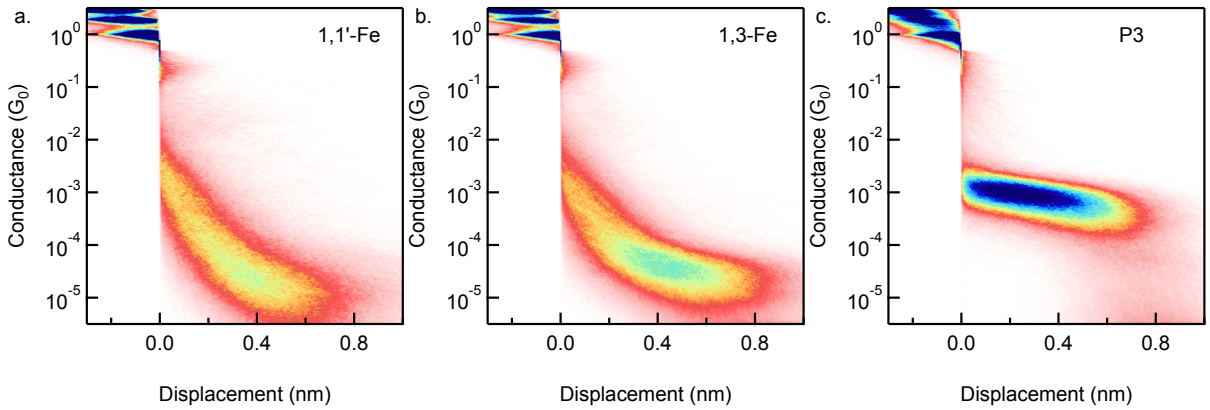

Fig. S1. Two-dimensional logarithmically-binned histograms for **a. 1,1'-Fe**, **b. 1,3-Fe** and **c. P3**. Each histogram is compiled from 10000 traces without data selection. Histograms have 200 bins per nm along the x-axis and 89 bins per decade along the y-axis.

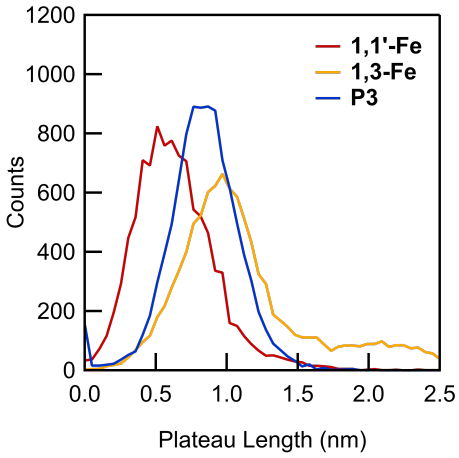

Fig. S2. Plateau length histograms were constructed by analyzing 10000 traces for each molecule. For each trace, the start and end of a plateau was determined by finding the displacement at which the conductance rose above or fell below the conductance of the molecular junction. Conductance limits used for **1,1'-Fe** and **1,3-Fe** junctions were 10^{-3} G_0 and 4×10^{-5} G_0. Conductance limits used for P3 junctions were 10^{-2} G_0 and 4×10^{-4} G_0. These limits were chosen to capture the majority of counts in conductance peak features determined from the 1D histograms shown in Fig.1b.

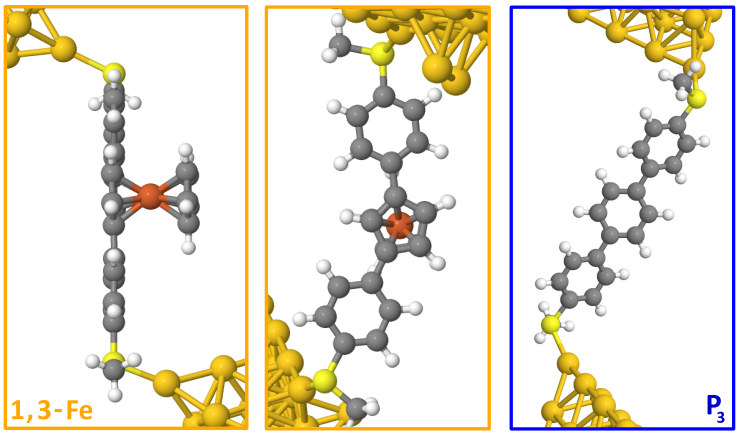

Fig. S3. Optimized junction geometries of **1,3-Fe** (side and top view) and **P3** (top view) used for the quantum transport calculations presented in Fig. 2b of the main paper.

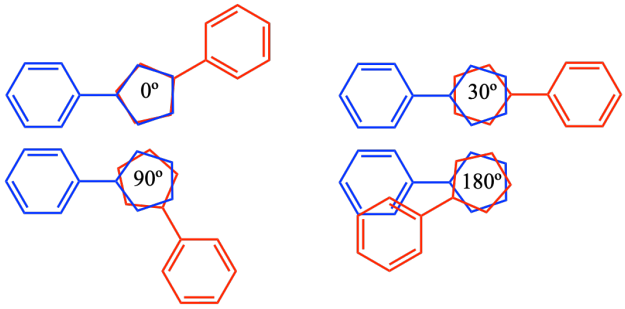

Fig. S4. **1,1'-Fe** with different relative angles (SMe and Fe not shown). Note that 0° is the relaxed geometry.

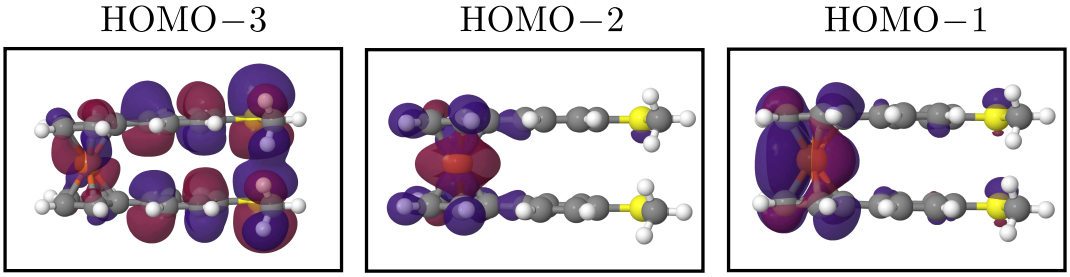

Fig. S5. Isosurface plot of the Kohn-Sham orbitals HOMO−3, HOMO−2 and HOMO−1 of the gas-phase molecule **1,1'-Fe** for the angle $\varphi \simeq 150°$ at which the distance between the SMe groups is minimal. The HOMO−3 orbital shows substantial overlap between the phenyl arms of the molecule and between the SMe groups.

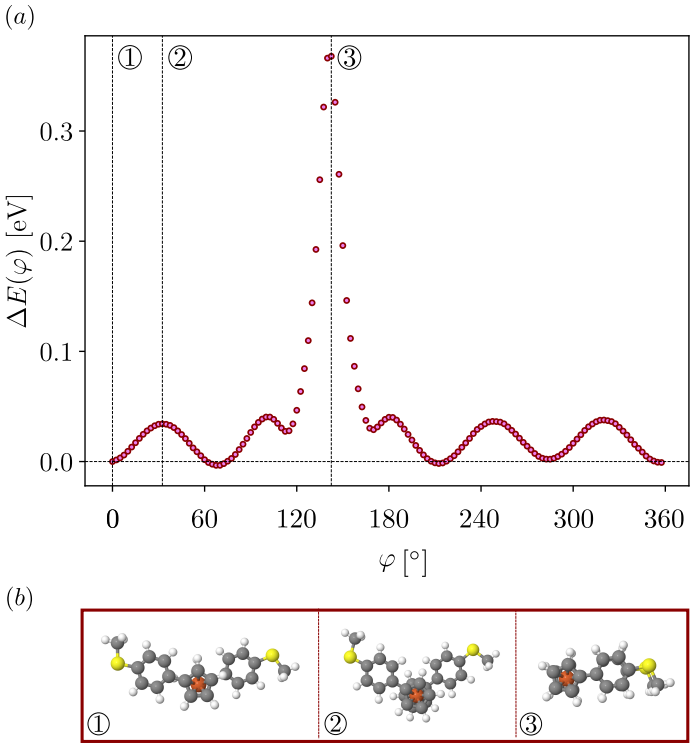

Fig. S6. (a) Energy cost due to ring rotation in isolated **1,1'**-Fe molecules. Energies are normalized to the total energy of the optimized gas-phase DFT calculation and angles defined according to Fig. S4. (b) Selection of geometries corresponding to the molecular configurations marked in panel (a) with dashed vertical lines. The geometry where the distance between SMe groups is minimal (given by ③) has a large energy barrier of ~ 365 meV with respect to the ground-state optimized geometry.

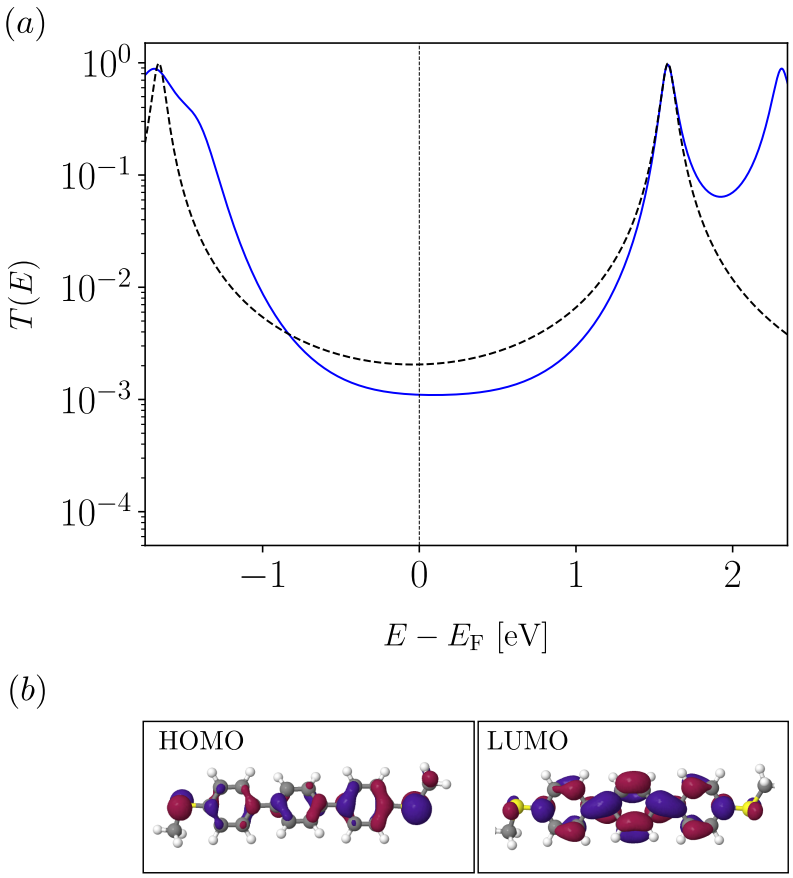

Fig. S7. (a) Comparison between the *ab initio* (blue continuous line) and the model (black dashed line) transmission function for **P3**. The toy-model transmission employs Eqs. (1)-(3) from the main text and we consider constructive interference between the HOMO-LUMO orbitals. The broadenings for both resonances are obtained from a fit of the well-defined LUMO resonance to Eq. (2) (which gives $\gamma_L = 0.13$ eV, $\gamma_R = 0.27$ eV). (b) According to our model, constructive interference occurs because the phase shift of the orbitals which participate is $\psi_{\mathrm{HOMO-LUMO}} = \pi$ as it can be observed by inspection of the amplitude at the S atom in the Kohn-Sham states of the isolated molecule.

ORBITAL SYMMETRY ANALYSIS

By looking at the Kohn-Sham states in Fig. S8, we see that independently of the rotation angle, φ, HOMO$-$2 and HOMO$-$1 tend to be strongly localized in the central ferrocene motif. Consequently, they manifest in the transmission as sharp Fano resonances [see Fig. 3 (b) in the main text]. For HOMO$-$2, the reason for the strong localization is the d_{z^2} spatial symmetry at Fe which prevents the overlap with the Cp π-system. In the case of HOMO$-$1, the d_{xy} orbital symmetry at the metal produces a δ-type bond with the Cp π-system such that a node is located at the carbon atom connecting to the phenyl linker so that the coupling to the electrodes remains weak. The other orbitals (HOMO$-$3, HOMO and LUMO) are significantly less localized and will give rise to the dominating transport resonances. Also here the symmetry analysis can be been done and we find that the d-orbital at the Fe core has corresponding symmetries d_{yz} (HOMO$-$3), $d_{x^2-y^2}$ (HOMO) and d_{xz} (LUMO). The delocalization of HOMO is due to $d_{x^2-y^2}$ having overlap with the ligands if, for HOMO$-$1, d_{xy} does not. Finally, hybridization of the remaining d-orbitals with a Cp ring benefits from the fact that the π-system of a single Cp ring itself exhibits a nodal structure that partially matches the two-lobes coming from d_{yz} and d_{xz} (π-bonding).

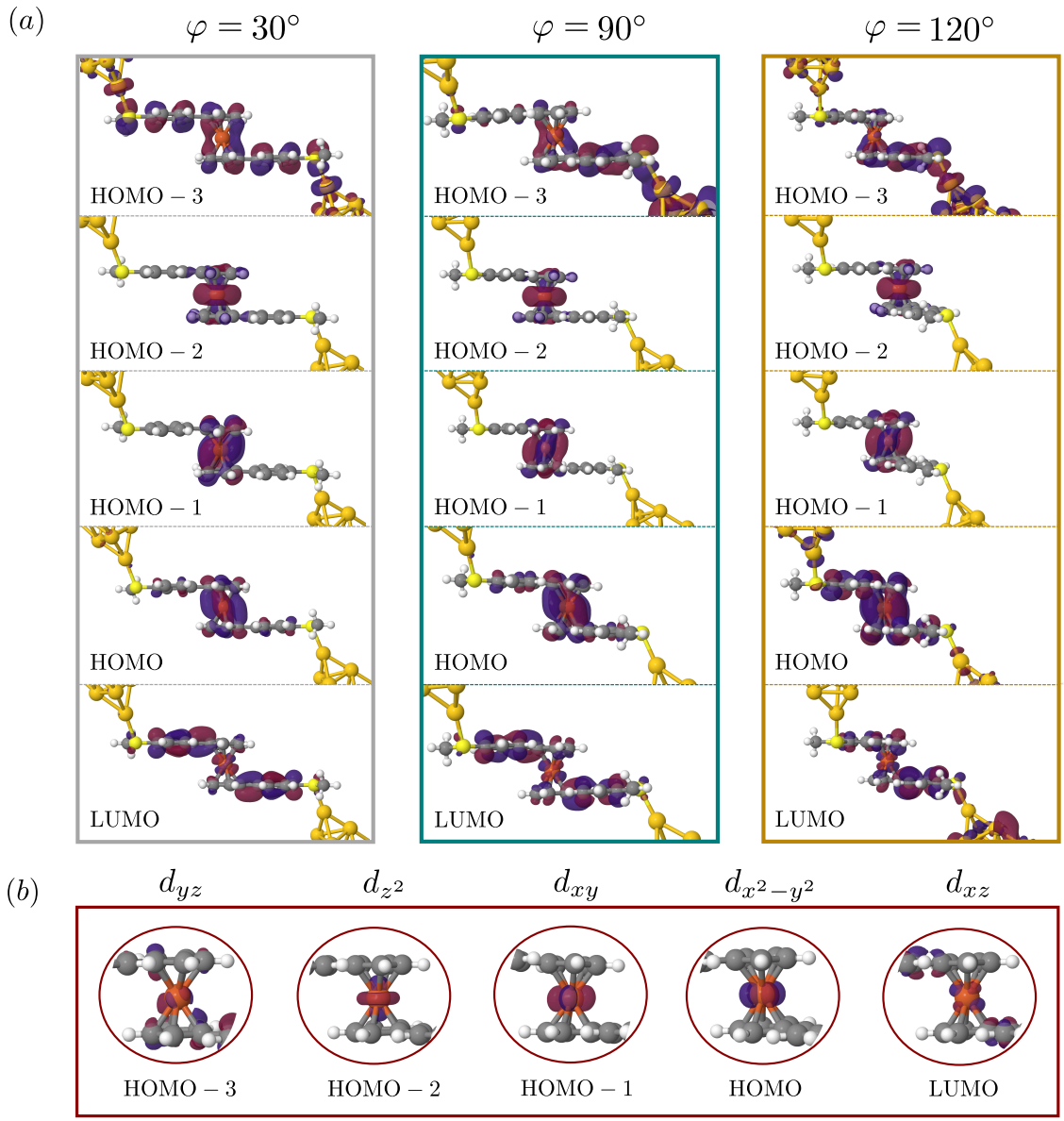

Fig. S8. (a) Selection of isosurface plots of the Kohn-Sham orbitals for the **1,1'-Fe** junction close to the Fermi energy. (b) Zoomed-in view of the scattering states for all orbitals shown in panel (a) for $\varphi = 90°$. The isosurface exhibits the d-orbital symmetry.

NMR SPECTRA

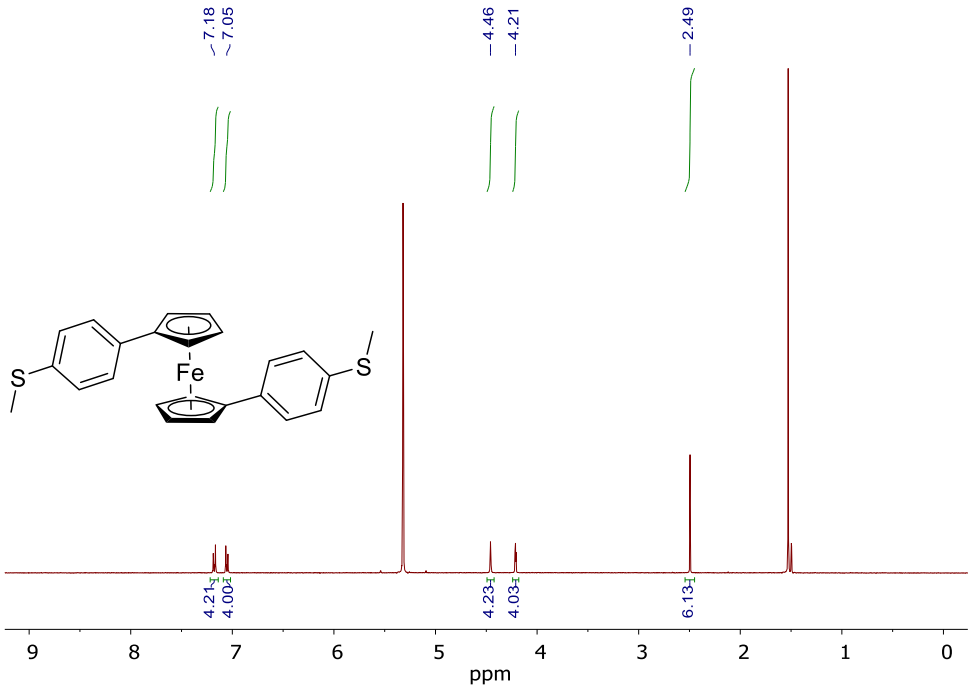

^{1}H NMR spectrum of **1,1-Fe** in CD_2Cl_2.

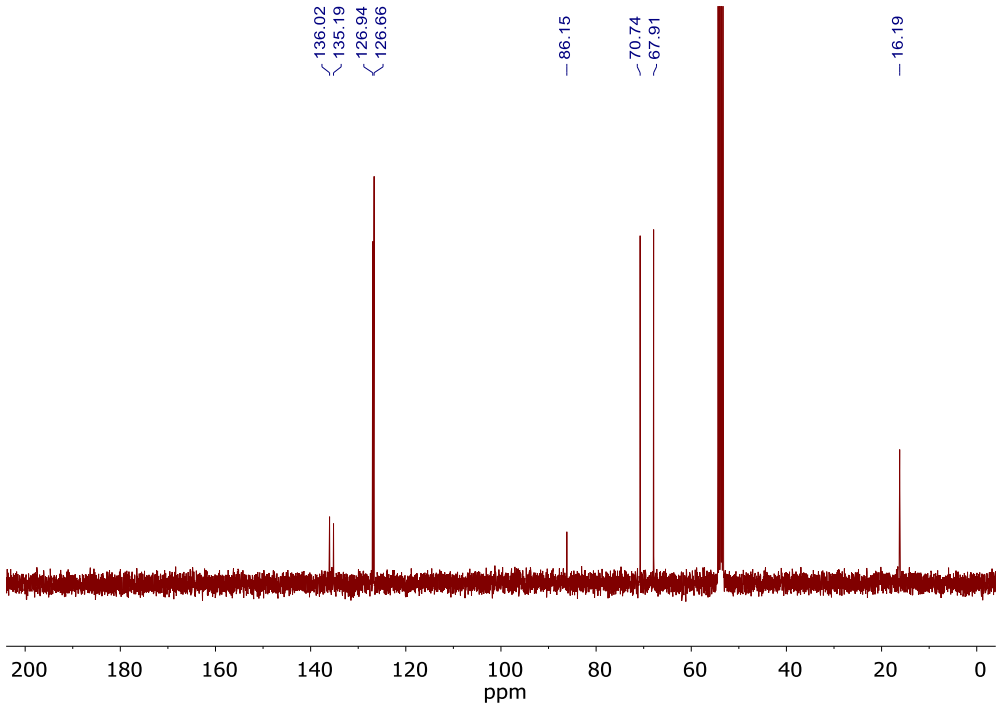

^{13}C{^{1}H} NMR spectrum of **1,1-Fe** in CD_2Cl_2.

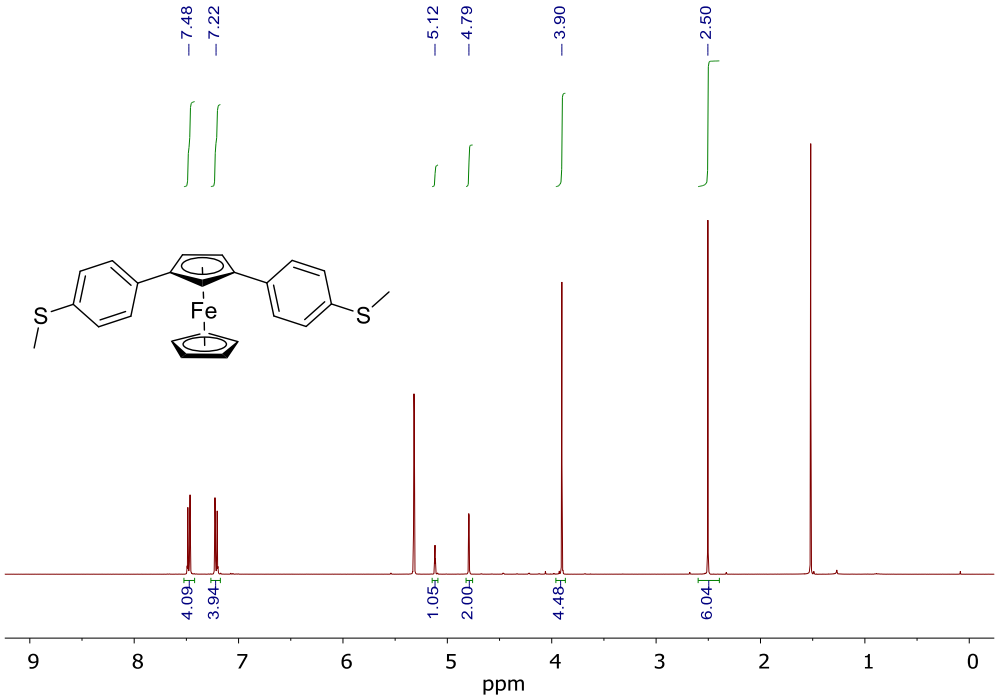

^{1}H NMR spectrum of **1,3-Fe** in CD_2Cl_2.

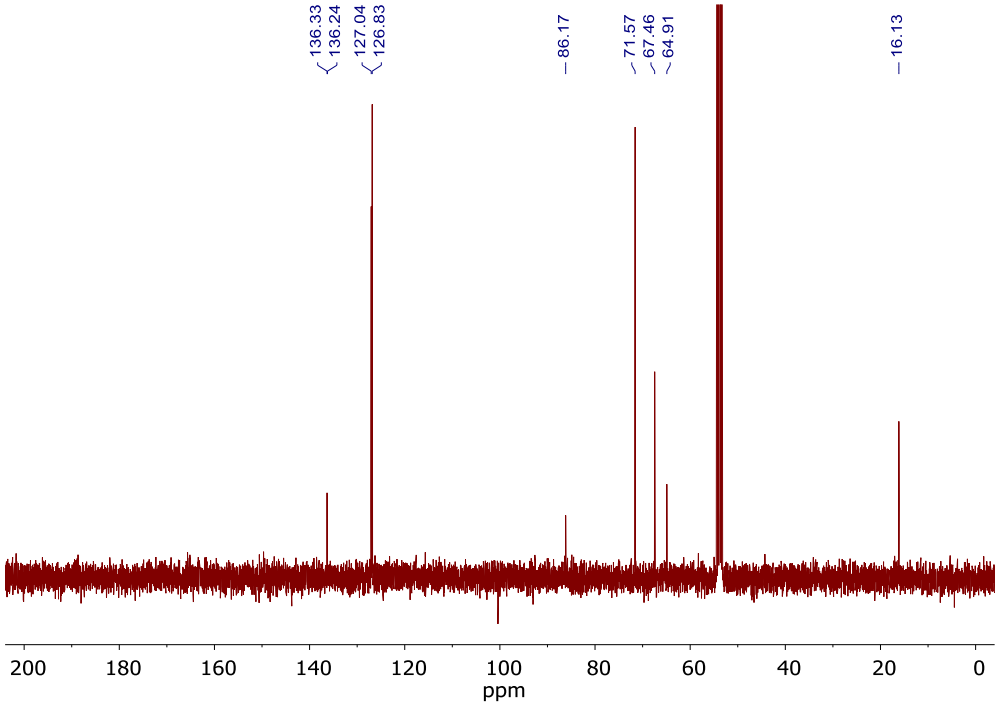

^{13}C{^{1}H} NMR spectrum of **1,3-Fe** in CD_2Cl_2.

[1] A. Zirakzadeh, A. Herlein, M. Groß, K. Mereiter, Y. Wang, and W. Weissensteiner, Organometallics **34**, 3820 (2015).

[2] H. V. Nguyen, M. Motevalli, and C. J. Richards, Synlett **2007**, 725 (2007).

[3] S. P. H. Mee, V. Lee, and J. E. Baldwin, Ang. Chem. Int. Ed. **43**, 1132 (2004).

[4] M. Enders, G. Kohl, and H. Pritzkow, Organometallics **21**, 1111 (2002).

[5] H. K. Cotton, F. F. Huerta, and J.-E. Bäckvall, Eur. J. Org. Chem. **2003**, 2756 (2003).

[6] G. K. Friestad, B. P. Branchaud, W. Navarrini, and M. Sansotera, "Cesium fluoride," in *Encyclopedia of Reagents for Organic Synthesis* (American Cancer Society, 2007).

[7] L. Venkataraman, J. E. Klare, I. W. Tam, C. Nuckolls, S. M. Hybertsen, and M. L. Steigerwald, Nano. Lett. **6**, 458 (2006).

[8] V. Blum, R. Gehrke, F. Hanke, P. Havu, V. Havu, X. Ren, K. Reuter, and M. Scheffler, Comput. Phys. Comm. **180**, 2175 (2009).

[9] J. P. Perdew, K. Burke, and M. Ernzerhof, Phys. Rev. Lett. **77**, 3865 (1996).

[10] E. v. Lenthe, E. J. Baerends, and J. G. Snijders, J. Chem. Phys. **99**, 4597 (1993).

[11] A. Arnold, F. Weigend, and F. Evers, J. Chem. Phys. **126**, 174101 (2007).

[12] A. Bagrets, J. Chem. Theory Comput. **9**, 2801 (2013).